Analytica Chimica Acta 1385 (2026) 345022

Contents lists available at ScienceDirect

Analytica Chimica Acta

journal homepage: www.elsevier.com/locate/aca

Electrochemically modulating the geometry of gold nanostructures for enhanced electrochemistry and antifouling performance

Feixiong Chen [a,b,*], Bahar Mostafiz [b], Emilia Peltola [b,**]

[a] Disease Networks Research Unit, Faculty of Biochemistry and Molecular Medicine, University of Oulu, 90014, Oulu, Finland
[b] Department of Mechanical and Materials Engineering, University of Turku, 20014 Turku, Finland

HIGHLIGHTS

- A unifying relationship between the electroactive surface area and electrochemical behavior across various gold nanostructure-modified electrodes was discovered.
- The nanostructure itself is the dominant determinant of both anti-fouling performance and electrochemical properties.
- Distinct growth mode of pine-needle-shaped GNS under the pulsed-wave deposition was observed compared to that fabricated by constant potential deposition.

GRAPHICAL ABSTRACT

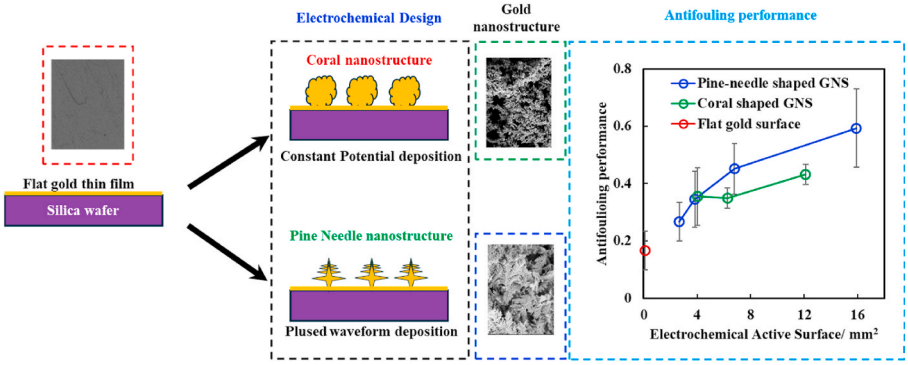

ARTICLE INFO

Handling Editor: Prof Lin Yuehe

Keywords:
Gold nanostructures (GNS)
Electrochemical deposition
Electrochemical sensing
Biofouling
Electrochemical design

ABSTRACT

Background: Biofouling, caused by nonspecific adsorption of biomolecules, compromises electrochemical sensor performance by blocking surface access and reducing sensitivity and reproducibility. Surface nanostructuring offers an effective route to counteract this effect and improve sensor reliability in complex biological media. However, their contributions to antifouling performance, caused by increases in electroactive surface area or the complexity of structured morphologies, have not been systematically investigated.

Results: We report a tuneable electrodeposition-based strategy to engineer gold nanostructures (GNS) with distinct geometries. Constant potential deposition (CPD) produced coral-shaped GNS, while pulsed-wave deposition (PWD) generated pine-needle-shaped GNS through a distinct anisotropic growth mode. Morphologies were confirmed by SEM, XPS, XRD, and water contact angle analysis. Electrochemical characterization (CV, SWV, EIS) revealed enhanced redox behaviour and reduced impedance in all GNS-modified electrodes compared to the unmodified gold-based screen-printed electrode (SPE). Pine-needle GNS demonstrated superior antifouling performance, retaining 59 % redox signal in bovine serum albumin, compared to 43 % for coral-shaped GNS. Crucially, by using a stepwise surface engineering approach with minimal variation in material composition, we demonstrated that nanostructure geometry, not just surface area, is the dominant factor governing both

* Corresponding author. Disease Networks Research Unit, Faculty of Biochemistry and Molecular Medicine, University of Oulu, 90014, Oulu, Finland.
** Corresponding author. Department of Mechanical and Materials Engineering, University of Turku, 20014 Turku, Finland.
E-mail addresses: feixiong.chen@oulu.fi (F. Chen), emilia.peltola@utu.fi (E. Peltola).

https://doi.org/10.1016/j.aca.2025.345022
Received 2 October 2025; Received in revised form 21 November 2025; Accepted 15 December 2025
Available online 17 December 2025

antifouling behaviour and electrochemical performance. A unifying relationship between electroactive surface area (ESA) and redox response was also observed across all GNS types.
Significance: This study highlights nanostructure shape as a key design parameter for enhancing sensor performance in biological environments. The modular deposition approach provides a robust platform for fabricating antifouling, high-sensitivity electrodes. These findings support future development of electrochemical sensors for clinical diagnostics and point-of-care applications.

1. Introduction

Electrochemical sensors are among the most versatile sensing techniques, offering significant value across diverse fields such as food safety monitoring [1], environmental analysis [2], and medical diagnostics [3–5]. Their widespread applicability stems from inherent advantages, including high sensitivity, rapid analysis, ease of miniaturization, and low cost. Among the electrochemical sensors, electrodes function as the central sensing component, serving as the interface where biorecognition events occur and translating these interactions into measurable redox signals via electrochemical processes [6,7] However, when electrodes are exposed to biofluids, especially in complex clinical samples such as plasma, urine, whole blood, or sweat, biofoulant molecules can adsorb onto the electrode surface through nonspecific binding or physical interactions. This leads to elevated background signals and diminished sensor sensitivity, and reproducibility [8]. Despite ongoing advances, the biofouling phenomenon remains one of the most persistent and critical challenges hindering the reliable application of electrochemical sensors in biological environments.

To ensure reliable detection in clinical settings, a range of antifouling strategies has been developed to mitigate the effects of biofouling in electrochemical sensors. These include surface modification with antifouling molecules[9–11], coating or adsorption of polymeric membrane [12], and the use of nanostructured materials [7,13–15]. Among these approaches, the use of nanostructured materials to engineer electrode surfaces has gained particular attention. This is not only due to their improved antifouling capabilities but also their ability to significantly increase the electroactive surface area (ESA), thereby enhancing the overall sensitivity and performance of the sensors.

Gold nanomaterial-functionalized interfaces offer high biocompatibility, excellent electrical conductivity, and an increased ESA, enabling greater probe loading and enhanced signal output. As a result, there is growing interest in engineering diverse gold nanostructures (GNS) on the electrode surfaces to improve both electrochemical performance and antifouling properties [14,16,17]. Among the available fabrication techniques, electrodeposition stands out as a reproducible and practical method for developing nanostructured gold on electrode surfaces. This approach allows for the fast and cheap creation of a wide variety of GNS morphologies, including flowerlike gold microstructures [18], hierarchical gold microstructures [19–21], gold nanoplates [22], gold nanowires [16], dendrite GNSs [23,24] and gold nanoparticles [25,26]. Interestingly, electrochemical methods enable the recovery of gold from complex feedstocks [27], paving the way for more sustainable extraction processes.

Although nanostructuring of gold surfaces to increase the ESA can significantly improve the sensing performance of electrochemical sensors, it also provides a challenge: a larger ESA may provide more sites not only for target analyte binding but also for nonspecific adsorption of background proteins and other fouling agents. This elevated susceptibility to biofouling can, in turn, compromise sensitivity and reduce the overall reliability of the sensor in complex biological environments. However, due to the size disparity between the analyte (a small molecule) and biofoulants (typically large biomolecules), the relationship between ESA and biofouling tendency is not straightforward and cannot be easily predicted. Additionally, as various analytes have diverse adsorption behaviors, this too adds complications to the issue of predicting the biofouling effect. Therefore, it is essential to systemically investigate how the ESA influences both the electrochemical behaviour and antifouling performance of GNS-functionalized electrodes.

Previously, researchers were mainly concerned with introducing novel morphologies of gold surfaces via the electrodeposition [23,26,28], or they focused on introducing Au electrode surfaces with high ESA [14,17] in sensor design. Although both criteria are widely used as indicators of antifouling performance, a gap remains in understanding how ESA and morphology differentially influence biofouling behaviour and, in particular, which parameter serves as the primary factor governing antifouling performance. In this study, we address this gap by clarifying the relationship between ESA, nanoparticle morphology, and their respective contributions to overall antifouling behaviour. On the other side, such a study will help clarify whether the nanostructures effectively hinder the diffusion of unwanted fouling proteins, while also assessing the potential trade-off, namely, the risk that the same structural features may impede the access of target analytes.

Herein, this work aims to investigate how variations in the geometry of GNS influence both electrochemical sensing performance and resistance to biofouling. Morphology of the crystals and rate of growth can be significantly affected by the electrochemical conditions, such as the current density, electrode potential, and the presence of impurities, leading to different crystal shapes and sizes [29]. To simplify the experimental design, two approaches of constant potential deposition (CPD) and pulsed-wave deposition (PWD) were used to fabricate the distinct gold nanostructures. As illustrated in Scheme 1, we have demonstrated the electrochemical design of two complex and hierarchical GNS morphologies, namely coral-shaped GNS and pine-needle-shaped GNS. Although simply adjusting the applied potential or deposition time can modulate the geometry of gold, they can also change the ESA of each sample, resulting in the diversity of ESA among the tested electrodes. Thus, to normalize the data analysis for all of the electrodes, we choose the ESA as an indicator for each electrode, regardless of their deposition time and applied potentials. Except for that, we mainly focused on the impact of these distinct electrodeposition strategies on electrochemistry and antifouling performance, because the different strategies enabled precise control over GNS growth and resulted in well-defined structures on the electrode surface. Our findings indicate that tailoring electrode surface morphology can significantly reduce biofouling while preserving high electrochemical performance, eliminating the need for additional antifouling coatings. Furthermore, the resulting nanostructured electrodes demonstrated improved precision, sensitivity, and quantitative reliability, supporting their potential for integration into point-of-care diagnostic platforms.

2. Experimental

2.1. Chemicals and apparatus

Gold (III) chloride trihydrate ($HAuCl_4{\cdot}3H_2O$), hexaammineruthenium(III) chloride ($[Ru(NH_3)_6]Cl_3$), potassium hexacyanoferrate(II) trihydrate ($K_4Fe(CN)_6{\cdot}3H_2O$), potassium ferricyanide ($K_3Fe(CN)_6$), sulfuric acid 98 % (H_2SO_4), sodium chloride (NaCl), disodium phosphate (Na_2HPO_4) and bovine serum albumin (BSA), were purchased from Sigma Aldrich. Potassium chloride (KCl) and potassium dihydrogen phosphate (KH_2PO_4) were acquired from VWR. Deionized (DI) water was produced by Milli-Q, Millipore, with the resistivity 18.2 MΩ•cm (Billerica MA). All chemicals were used as received without any further

purification.

Platinum (Pt) wire (diameter 0.5 mm, 99.99 %) and gold-coated silicon wafer (GSW, 99.999 % Au, layer thickness of 100 nm) were purchased from Sigma Aldrich as well, serving as a counter electrode and working electrode, respectively. Two Ag/AgCl reference electrodes were used in this study, to be used in different buffers (aqueous solution and H_2SO_4 solution). The first, labelled as RE-1, was a porous Teflon-tip Ag/AgCl reference electrode (CHI111) acquired from CH Instruments, Inc. (USA). It was specifically employed for the electrodeposition process in sulfuric acid solution. The second electrode, labelled RE-2, was a refillable Ag/AgCl reference electrode (6.0 mm diameter, 70 mm length) obtained from redox.me (Sweden). This electrode was used for detection in phosphate buffer saline (PBS) solution.

The PBS solution was prepared by dissolving 80 g NaCl, 2.0 g KCl, 14.4 g Na_2HPO_4, and 2.4 g KH_2PO_4 in 10.0 L of DI water with a final pH of 7.4. The purchased sulfuric acid was diluted to different concentrations (H_2SO_4 50.0 mM, 0.5 M, and 1.0 M) in DI water. 10.0 mM of $HAuCl_4$ solution was freshly prepared by dissolving 473.0 mg of $HAuCl_4{\cdot}3H_2O$ in 120.0 mL of 1.0 M H_2SO_4. For biofouling testing, the preparation of solutions was conducted with precision to meet experimental requirements. A 3.0 mM [$Ru(NH_3)_6^{3+}$] solution was freshly prepared as the outer sphere redox (OSR) probe solution by dissolving [$Ru(NH_3)_6$]Cl_3 in PBS, into which BSA was added at a concentration of 40.0 mg•mL^{-1}. Similarly, the inner sphere redox (ISR) probe solution was prepared by dissolving $K_4Fe(CN)_6{\cdot}3H_2O$ in PBS to achieve a 3.0 mM [$Fe(CN)_6^{4-}$] solution, followed by the addition of BSA at a concentration of 2.0 mg•mL^{-1}. These carefully prepared solutions ensured the reliability of biofouling tests under controlled conditions.

2.2. Gold electrode (GE) fabrication

Firstly, gold-coated silicon wafer was hand-cut into smaller segments, measuring around 1.0 cm^2. And it was then contacted to Cu slabs with a conductive copper tape (with resistance through adhesive <1 Ω, 3 M Electrical Markets Division, UK). Secondly, following our previous fabrication method [30,31], the inert polytetrafluoroethylene (PTFE) film tape (Irpola, Finland) was punched with a hole with a 2.0 mm diameter, which was placed on top of the gold-coated silicon wafer to define the working area of the electrode of 2.0 mm. Lastly, the remainder of the electrode was covered and sealed with polytetrafluoroethylene (PTFE) tape, so as to isolate the copper from the electrolyte. The image of the fabricated electrode was presented in Fig. S1, and the geometric surface area of the electrode was defined by exposing a 2.0 mm diameter hole. All the fabricated GEs were washed with isopropanol for three times followed by rinsing with DI water three times. After drying, each GE was checked by the ohmmeter to confirm its resistance was <1 Ω.

2.3. Electrochemical deposition of varying GNS

All the GEs were immersed in 40.0 mL of $HAuCl_4$ 10.0 mM solution. The electrochemical deposition was performed using a Palmsens EmStat4 potentiostat in a three-electrode configuration with an Ag/AgCl reference electrode (RE-1), a Pt counter electrode (Pt wire), and the fabricated GE. For the electrochemical deposition process, two methods were used (as shown in Fig. S2): **1)** CPD and **2)** PWD. In CPD, a fixed potential (e.g., CPD@0V, CPD@-0.3V, CPD@-0.7V, CPD@-1.0V, CPD@-2.0V, CPD@-3.0V, CPD@-4.0V, CPD@-5.0V, and CPD@-6.0V) was applied in the deposition times of 120 s or 400 s. In PWD, a square waveform was used, where the t for −0.7V (PWD@-0.7V) or −1.2V (PW@-1.2V) was 2 ms, and the t for +1.2 V was 1 ms, under a running time of 120 s and 400 s. After CPD or PWD, a chronoamperometric step at −1.2 V was finally applied for 10 s to reduce gold oxides on each GE.

2.4. Characterization of ESA

The ESA of GEs was quantified electrochemically using cyclic voltammetry (CV). These values were calculated based on the charge of the reduction peaks in CVs obtained in 50.0 mL of H_2SO_4 (50.0 mM) solution. The potential window was set from 0 V to 1.4 V, with a scan rate of 100 mV•s^{-1}. ESA was determined by integrating the current peak of the gold oxide reduction, using a charge density of 386 μC•cm^{-2} [32], corresponding to a complete monolayer of gold oxide. Several samples were prepared (N ≥ 3), where each sample was run for three cycles of CV.

2.5. Characterization of electrochemical performance and biofouling behaviour

Electrochemical performance of each GE was measured in 3.0 mM [$Ru(NH_3)_6^{3+}$] and 3.0 mM of [$Fe(CN)_6^{4-}$] (50.0 mL). The three-electrode system was composed of a Pt wire, an Ag/AgCl reference electrode (RE-2), and a GE as the working electrode. For all the measurements, the scan rates of SWV (step size of 0.01 V, amplitude of 0.05 V and frequency of 40.0 Hz) and CV (3 cycles) were 100 mV•s^{-1} in the potential range from −0.6 to 0.2 V and repeated for three cycles. The same cell configuration, electrochemical methods, and values were used for biofouling studies.

Our previous studies indicate that biofouling affects the redox kinetics of outer and inner sphere probes on carbon surfaces drastically differently [30,31]. Here, we investigated probes classically considered as outer-sphere probes. However, $Ru(NH_3)_6^{3+}$ is a *true* clean outer-sphere probe, while $Fe(CN)_6^{4-}$ is often considered outer-sphere, but it is more surface-sensitive, similar to the inner-sphere performance. Another noteworthy point is that since the isoelectric point of BSA is around pH 5, at pH 7.4 in PBS, the protein carries a net negative charge. Once adsorbed on the electrode, it could repel $Fe(CN)_6^{4-}$ while having little effect on, or even attracting the $Ru(NH_3)_6^{3+}$. Thus, for biofouling testing, 40.0 mg•mL^{-1} of BSA was dispersed in the 3.0 mM [$Ru(NH_3)_6^{3+}$], while 2.0 mg•mL^{-1} of BSA was dispersed in 3.0 mM of [$Fe(CN)_6^{4-}$]. Before each measurement, GE were immersed in the biofouling solution from 0 h to 40 h. Each sample was scanned by CV and SWV three times, and at least three or four GEs were prepared under each condition.

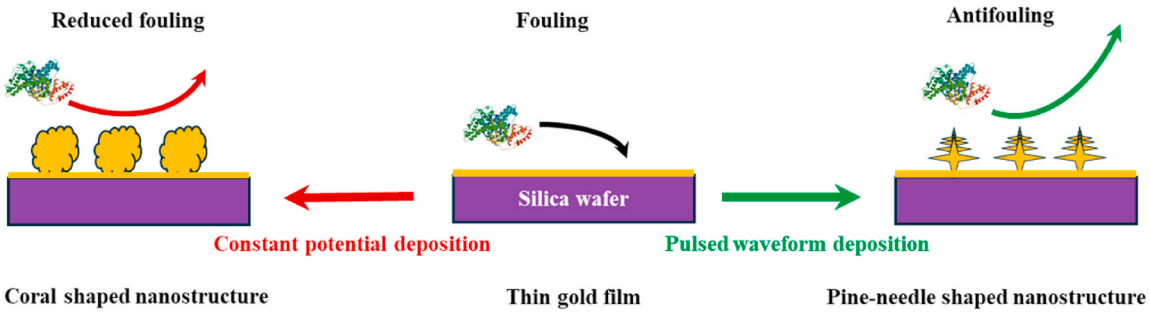

Scheme 1. Two electrochemical deposition strategies to design varying gold nanostructures on the gold electrode.

2.6. Surface characterization of SEM, XPS, XRD, and WCA

Scanning electron microscopy (SEM) was conducted via a Thermo Scientific FE-SEM Apreo S for surface imaging of GEs. X-ray photoelectron spectroscopy (XPS) analysis was performed with a ThermoFisher ESCAlab 250 imaging X-ray photoelectron spectrometer (Al Kα (1486.68 eV), 500 μm spot size, 50 eV pass energy, 0.1 eV step size). Crystallographic orientation of the deposited layers was assessed by X-ray diffraction (XRD) performed in Empyrean XRD from Malvern Panalytical, equipped with a Cu Kα source (λ = 1.5418 Å), in the 2θ window from 30° to 120°, using a scan step of 0.05°. Attension Theta Optical Tensiometer (Biolin Scientific, Japan) were used for water contact angle (WCA) measurements via the DI water droplets (5.0 μL).

3. Results and discussions

3.1. Relationship between ESA of GE and electrochemical performance

Electrochemical deposition strategies enable the formation of various surface morphologies on electrodes, which in turn influence differences in the ESA. Before examining the specific morphological features induced by the CPD and PWD, this section aims to first assess how an increase in the microscopic surface area impacts the overall electrochemical performance.

The ESA of varying GNSs was characterized using CV in a 50 mM H_2SO_4 solution, scanned from 0 to 1.4 V at a rate of 100 $mV \bullet s^{-1}$ (Fig. S3). As typically observed, the CV curves exhibited a distinct gold oxidation peak at 1.34 V, which is characteristic of the Au (111) crystallographic plane [33,34]. Fig. S4 summarizes the calculated ESA of GE and GNS-modified electrodes, derived from the H_2SO_4 reduction peak at 0.88 V in the CV curves. To allow direct comparison, deposition times of 120 s (Fig. S4A) and 400 s (Fig. S4B) were selected for both the CPD and PWD methods. Particularly, the ESA of the unmodified GE was measured to be 0.11 ± 0.02 mm^2, as a reference throughout the study.

At a deposition time of 120 s, ESA increased with more negative CPD deposition potentials (from −0.7 to −3.0V), ranging from 4.03 ± 0.88 mm^2 to 8.36 ± 1.06 mm^2. However, applying even more negative potentials (−3.0 to −6.0 V) using the CPD method did not result in further significant ESA enhancement. Similarly, at the deposition time of 400 s (Fig. S4B), the ESA increased as the CPD deposition potential was lowered from −0.3 to −2.0 V. Beyond −2.0 V (up to −4.0 V), the ESA plateaued, averaging around 29.5 mm^2. These results suggest that deposition voltage primarily influences the growth morphology of GNS, while deposition time determines the quantity of deposited material.

In addition to CPD, the PWD strategy was also employed to enhance the ESA of electrodes, as shown in Figure S3 (D and E). A comparison of ESA values at two deposition times is presented for PWD (red columns, Fig. S4A and S4B). At a deposition time of 120s, when the potential was lowered from −0.7 V to −1.2 V, the ESA increased from 2.68 ± 0.56 mm^2 to 3.84 ± 0.85 mm^2. In the longer deposition time of 400 s, the ESA rose more noticeably, from 6.80 ± 0.86 mm^2 at −0.7 V, to 15.90 ± 1.02 mm^2 at −1.2 V. These results suggest that, compared to the GE, the CPD method indicated more pronounced changes than the PWD method.

As we noted, the diversity of the ESA was caused by the adjustment of the various deposition conditions. To normalize the data analysis in this investigation, we mainly focused on the indicator of ESA for each electrode, rather than on their deposition conditions. Because the process time was kept the same for CPD and PWD. However, the effective deposition time differs because of the pulsed nature of PWD, which reduces the actual running time to about 66 %. In addition, during PWD, the applied positive potential (+1.2 V) introduces an etching effect. For this reason, it is not straightforward to determine the exact deposition time that would result in equal amounts of deposited material in both processes. Instead, we compared the trends based on the ESA. Indeed, for the same process time, the ESA is higher with CPD than with PWD, which is expected since in CPD the electrode remains at a strongly negative potential for longer durations.

An OSR probe of $[Ru(NH_3)_6^{3+}]$ and an ISR probe of $[Fe(CN)_6^{4-}]$, were used to investigate how ESA influences electrochemical behaviours. Fig. 1 displayed the relationship of various ESAs and their electrochemical responses, where the black data points were from these electrodes fabricated by CPD and the red data points were from those of PWD, respectively.

Generally, we observed the relationship between ESA and the corresponding electrochemical response of the OSR probe $[Ru(NH_3)_6^{3+}]$ (Fig. 1A), regardless of their different deposition conditions. The maximum redox intensity was observed for an ESA of 2.68 ± 0.56 mm^2 (which was observed for PWD@-0.7V in this study, see Fig. S4A). The results show that as the ESA increased from GE to more complex GNS-modified electrodes, the electrochemical response correspondingly is enhanced. However, excessive deposition of GNS and an overly large ESA may lead to increased capacitive currents, which in turn reduce the redox signal intensity.

ISR probe reactions occur in close proximity to the electrode's surface. They are sensitive to the electrode's surface chemistry and strongly affected by specific interactions between the electrode surface and the redox species. Thus, Fig. 1B presents the electrochemical response of the ISR probe as a function of ESA from all tested samples fabricated by both CPD and PWD from this study, with the maximum intensity observed at 6.27 ± 1.20 mm^2 (as observed for CPD@-1.0V in Fig. S4A). However, the increase in ESA had a less pronounced impact on the electrochemical response of the ISR probe compared to that of the OSR probe.

Importantly, the two gold deposition methods of both CPD and PWD, exhibited no significant differences in the overall tendency of ESA-dependent responses for both OSR and ISR probes, as shown in Fig. 1. Our observations directly indicate that the electrochemical performance of the electrode followed a similar trend, primarily governed by the final value of ESA, regardless of the deposition strategy (e.g., CPD and PWD). Therefore, even if ESA played an important role in the electrochemical performance to some extent, merely a controlled increase of ESA seemed insufficient for any further improved electrochemical performance. Now, our study shifted from solely focusing on ESA values to investigating how morphological characteristics of GNS can have a meaningful impact on electrochemical performance.

3.2. Electrochemical modulation of the GNS geometry

To gain insight on the role of GNS morphological differences in electrochemical performance, we employed two distinct electrochemical deposition strategies, CPD and PWD, to produce geometrically different GNS structures. GNS morphology can be electrochemically modulated by simply programming the applied potential.

First, the original morphology of the unmodified GE was characterized in Fig. S5, featuring plated gold films. And Fig. S6 presents the CV and SWV curves for the unmodified GE.

Then, controlled gold deposition, using CPD and PWD strategies was carried out. The resulting morphologies of the modified GE surfaces were investigated (Fig. 2). Among these CPD samples, the morphology of deposited GNSs varied with the applied potentials [14,28,33]. Consistent with our previous study on screen-printed gold electrodes [7], we observed that lower CPD deposition potentials (0, −0.3, and −0.7V) yielded three distinct GNS morphologies: needle-shaped (Fig. 2A), leaf-shaped (Fig. 2B), and coral-shaped GNS (Fig. 2C), respectively. Fig. S7 provides SEM images at additional magnifications for each of these conditions.

In Fig. S6C, we further compared the effect of deposition time and potential under the CPD process on the redox response of $[Ru(NH_3)_6^{3+}]$ (1.0 mM). Among them, we observed GNS deposited at CPD@-0.7V for 400 s, allowing for the highest redox intensity. This suggests that lower CPD deposition potential (0 V to −0.7 V) may be insufficient for efficient gold deposition on GE.

To expand on these observations and develop more broadly

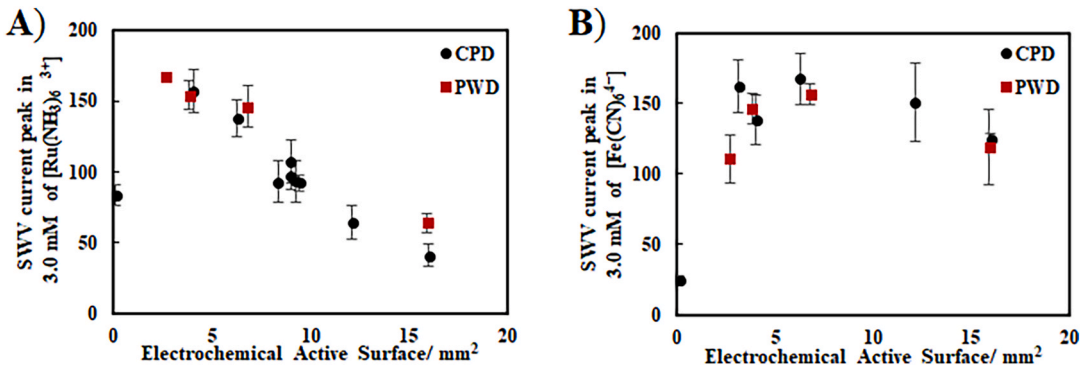

Fig. 1. Square wave voltammetry peak current response of the electrochemically active surface fabricated by constant potential deposition (CPD, Black dots)) and pulsed-wave deposition (PWD, Red dots). **A**) Measurements in 3.0 mM of $[Ru(NH_3)_6{}^{3+}]$ and **B**) measurements in 3.0 mM of $[Fe(CN)_6^{4-}]$. The gold nanostructure deposition conditions relevant to the electrochemically active surface are detailed in Fig. S3 and Table S1. (For interpretation of the references to colour in this figure legend, the reader is referred to the Web version of this article.)

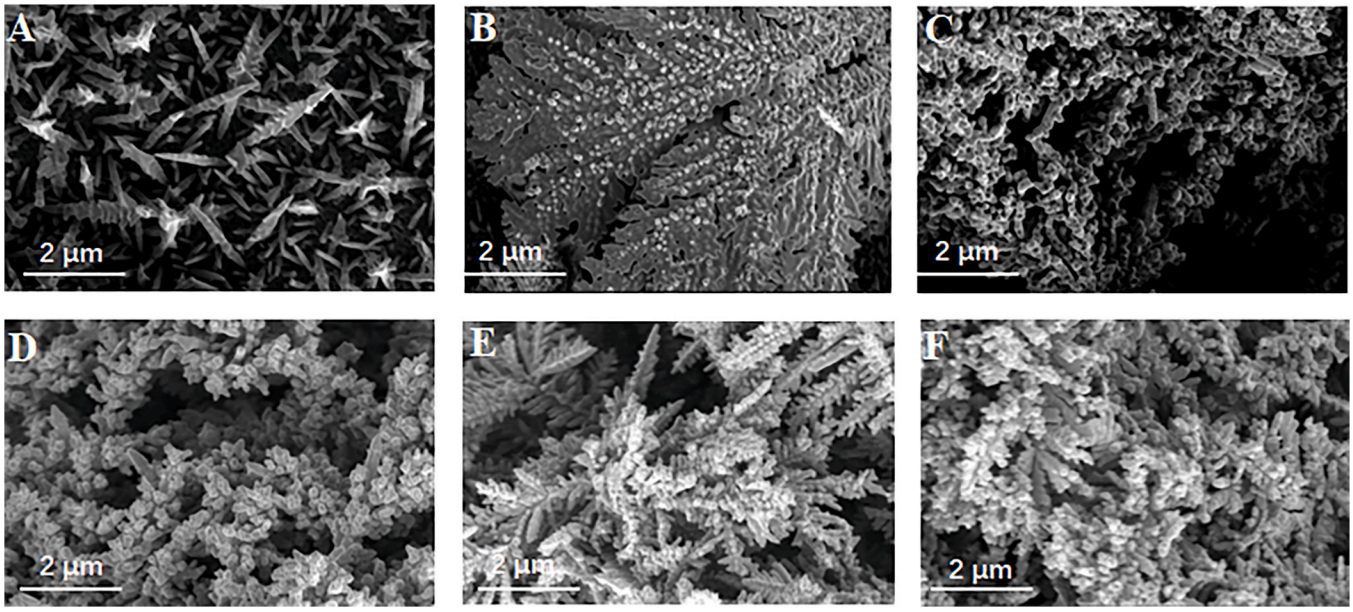

Fig. 2. Scanning electron microscopy image of as-prepared gold nanostructures on gold substrates fabricated using different deposition methods, **A)** CPD@0V, **B**) CPD@-0.3V, **C)** CPD@-0.7V, **D**) CPD@-1.0V, **E**) PWD@-0.7V, and **F**) PWD@-1.2V.

applicable GNS morphologies, we further examined gold deposition via CPD using higher negative CPD deposition potentials (from −1.0 to −3.0 V). As the CPD deposition potentials became more negative, however, the resulting structures showed no significant morphological changes. The SEM images in Fig. S8 reveal that the gold deposits exhibit a porous structure. Similar structures have been demonstrated with Cu and Sn deposits [35]. The formation of the porous structure can be attributed to gas bubbles that evolve at various substrate locations, acting as dynamic negative templates during metal deposition and resulting in foam-like structures. Pore size increases with distance from the substrate due to hydrogen bubble coalescence. The morphologies formed under the CPD deposition potentials between −1.0 and −3.0 V were not only similar to one another but also closely resembled the coral-shaped GNS formed at −0.7 V (Fig. 2C and D). The minimal difference in GNS size and the lack of pronounced microscale shape variation suggest that CPD has limited capacity to modulate the GNS growth at more negative deposition potentials. Thus, further studies were focused on the CPD@-0.7V sample, as a reference.

We further employed PWD method to explore alternative GNS morphologies. At a PWD deposition potential of −0.7 V, we observed the formation of pine-needles-shaped GNS (Fig. 2E). Unlike CPD, the PWD process (Fig. S2B) integrates both electrodeposition and electro-etching, a combination that likely promotes dendritic gold growth [14,28]. The SEM images (Fig. S9A) reveal that the central rods of the pine-needle-shaped GNS are ~10 μm in length, surrounded by uniformly distributed compact leaf-like structures that grow outward to encase each rod. These features are characteristic of the pine-needle-shaped GNS morphology.

At a more negative PWD deposition potential of −1.2 V, the second type of pine-needle-shaped GNS was formed (Fig. 2F). As shown in the SEM image (Fig. S9B), this potential enhances the development of gold branches, resulting in more densely packed, leek-like structures. The central rods in this PWD@-1.2V are ~5.0 μm in length. These observations indicate that as the PWD potential becomes more negative, the growth of pine-needle-shaped GNSs becomes increasingly stochastic.

Compared to the coral-shaped GNS fabricated by CPD (Fig. 2C and D), these PWD-designed GNS (Fig. 2E and F) exhibit pronounced differences in both micrometric and nanometric features. The distinct structural characteristics modulated by PWD allow for controlled nano-engineering of gold deposition outcomes, such as the collapse length of the central rod and the density of the branching structures [33]. Overall, the PWD strategy promotes the growth of gold dendritic branches, with

branch density increasing at more negative PWD deposition potentials. Notably, the PWD@-1.2V displays a rougher and more porous surface morphology on the GE, which is attributed to its smaller structural dimensions and the formation of denser branches compared to those of the initial PWD@-0.7V [33].

Based on the initial electrochemical and morphological studies, further studies were conducted with CPD@-0.7V, PWD@-0.7V and PWD@-1.2V, where the first two (CPD@-0.7V and PWD@-0.7V) share the same deposition potential and the first and last (CPD@-0.7V and PWD@-1.2V) share comparable ESA. The main focus is on samples deposited for 400 s. For comparison, we included data for GNS-modified electrodes deposited for 120 s, which yielded insufficient ESA and porosity, in the supplementary material of Fig. S4A.

3.3. Surface characterization of deposited GNS

Based on our previous study [7], the chemical state (XPS), crystal structure (XRD) or wettability (water contact angle) are not significantly different across diverse types of GNS morphologies. Therefore, we primarily characterized the surface of the GNS deposited at CPD@-0.7V as a representative example for comparison with the unmodified GE.

XPS was used to analyse the oxidation states of the gold on both unmodified GE and GNS based surfaces. The results indicate that the chemical states of Au species were identical in GE and GNS, with no additional Au-related peaks detected by XPS, suggesting similar atomic environments for gold in both samples (Fig. 3A). Table S2 presents the XPS core level spectrum, showing characteristic peaks at binding energies of 84 and 87.7 eV, corresponding to the chemical states of Au 4f7/2 and Au 4f5/2, respectively [36]. This confirms that the electrode surfaces are composed predominantly of metallic gold. Increased surface roughness or porosity can expose a greater relative proportion of non-gold elements (e.g., contaminants or residual reagents) or influence the sampling depth and signal attenuation in XPS analysis, potentially contributing to the lower apparent Au percentage, from 59.22 % in GE to 47.87 % in GNS.

XRD patterns of GE and deposited GNS are shown in Fig. 3B. The highly crystalline GE exhibits three characteristic diffraction peaks: those at 38.2° and 82.5° correspond to the Au (111) and (222) crystal orientations, respectively. In addition, a strong peak at 69.1° and a slightly less intense peak at 69.3° are attributed to Si(400) crystalline facets, originating from the silicon wafer substrate (full scale in Fig. S10) [37,38]. For the deposited GNS, additional XRD peaks appear alongside these existing reflections. New peaks observed at 44.4°, 64.7°, and 77.6° correspond to the Au(200), Au(220), and Au(311) crystalline planes, respectively [14,39].

As presented in Fig. 3C, the WCA (θ) of the unmodified GE was 83.9 ± 0.1°. Following GNS formation, the WCA increased to 144.7 ± 0.02°, demonstrating a marked enhancement in surface hydrophobicity as a result of the deposition process [17]. Pronounced hydrophobicity is a property known to correlate with antifouling performance [40]. Thus, hydrophobicity can partly account for the differing biofouling performance observed between the flat surface and the GNS structures. Within the GNS structures themselves, however, other factors, such as thin-layer effects, altered mass transport, and local electrostatic environments, are more likely to play dominant roles.

Overall, the surface characteristics of the electrochemically deposited GNS demonstrated substantial alterations compared to those of the unmodified GE.

3.4. Electrochemical performance of GNS based GEs

Based on the preliminary testing, we focused primarily on fabricating GNSs under the more negative deposition potentials of −0.7 or −1.2 V, by using both CPD and PWD methods. Table 1 summarizes the electrochemical performance using $[Ru(NH_3)_6^{3+}]$ and $[Fe(CN)_6^{4-}]$ as redox probes, on the following electrode types: **i)** GE, **ii)** CPD@-0.7V, **iii)** PWD@-0.7V and **iv)** PWD@-1.2V.

The ΔE_p values obtained from CV were compared across all tested electrodes, as ΔE_p serves as an indicator of the electron transfer kinetics. By using $[Ru(NH_3)_6^{3+}]$, this OSR probe reaction exhibited the following electron transfer kinetics on each electrode type: GE ($\Delta E_p = 77 \pm 6$ mV), CPD@-0.7V ($\Delta E_p = 54 \pm 3$ mV), PWD@-0.7V ($\Delta E_p = 50 \pm 4$ mV) and PWD@-1.2V ($\Delta E_p = 50 \pm 5$ mV). In addition, the I_{pa}/I_{pc} ratios were calculated to be 0.87 ± 0.04 for GE, 0.80 ± 0.04 for GNS (CPD@-0.7V), 0.90 ± 0.05 for PWD@-0.7V, and 0.87 ± 0.13 for PWD@-1.2V, respectively. Based on the ΔE_p values below 100 mV, the I_{pa}/I_{pc} ratios close to 1 (0.8–0.9), the electrochemical reaction of $[Ru(NH_3)_6^{3+}]$ can be considered reversible on GNS-modified electrodes.

Interestingly, GE exhibited an irreversible behaviour by using the ISR probe of $[Fe(CN)_6^{4-}]$. Although the I_{pa}/I_{pc} value was close to 1 (0.94 ± 0.13), the ΔE_p was significantly higher than 100 mV ($\Delta E_p = 224 \pm 11$ mV). In contrast to the sluggish kinetics observed on GE, the GNS-modified electrodes showed enhanced electrochemical performance, attributed to their increased roughness [41] and porosity [42]. The ΔE_p of GNS-modified electrodes CPD@-0.7V, PWD@-0.7V and PWD@-1.2V were narrower, 57 ± 8, 63 ± 5, and 62 ± 5 mV, respectively. However, despite ΔE_p values below 100 mV, the higher I_{pa}/I_{pc} value (ranging from 1.25 ± 0.04 to 1.62 ± 0.12) suggests that the reaction is non-ideal on these surfaces. This behaviour is consistent with previous studies showing that porous and rough electrodes can exhibit non-ideal I_{pa}/I_{pc} ratios due to capacitive contributions and adsorption effects, even when

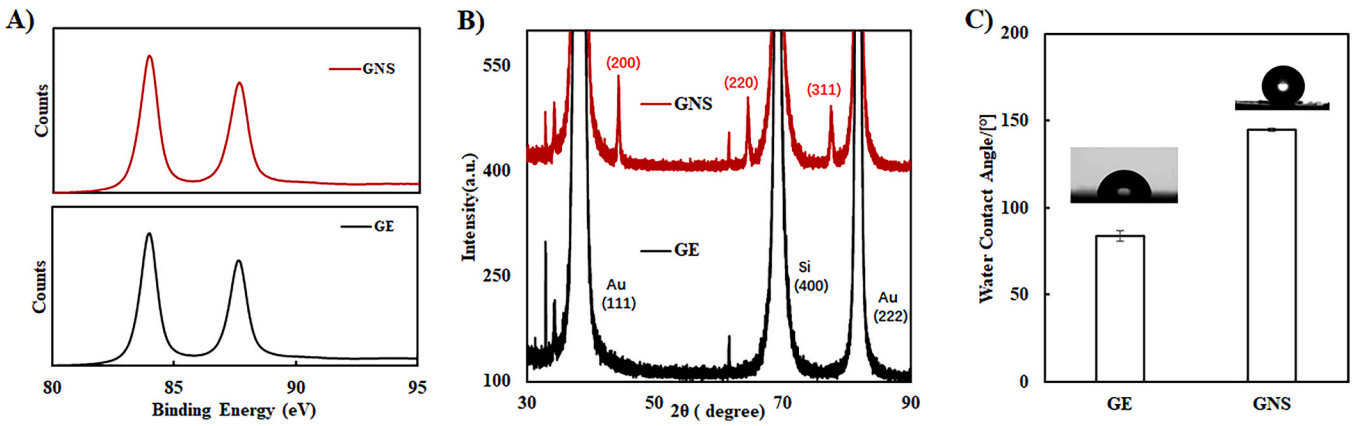

Fig. 3. Surface characterization of unmodified gold electrode (GE) and gold nanostructure (GNS) modified electrode (CPD@-0.7V(400s)). **A)** XPS spectra, **B)** XRD patterns recorded from 30° to 90° using Cu Kα X-ray (1.54 Å), **C)** Water contact angle measurement. (For interpretation of the references to colour in this figure legend, the reader is referred to the Web version of this article.)

Table 1
Electrochemical performance of unmodified gold electrode (GE) and gold nanostructure modified electrodes (CPD@-0.7V, PWD@-0.7V and PWD@-1.2V) with and without the presence of bovine serum albumin (BSA). Biofouling is measured after 0.5 h exposure.

Electrodes	Biofouling	3.0 mM $[Ru(NH_3)_6^{3+}]$			3.0 mM $[Fe(CN)_6^{4-}]$		
		ΔE_p/mV	I_{pa}/μA	I_{pa}/I_{pc}	ΔE_p/mV	I_{pa}/μA	I_{pa}/I_{pc}
GE/Unmodified	**No BSA**	77 ± 6	11.5 ± 1.2	0.87 ± 0.04	224 ± 11	9.3 ± 1.8	0.94 ± 0.13
	BSA	74 ± 3	10.9 ± 1.1	0.91 ± 0.00	–	–	–
CPD@-0.7V	**No BSA**	54 ± 3	18.6 ± 0.2	0.80 ± 0.04	57 ± 8	23.4 ± 4.3	1.62 ± 0.12
	BSA	60 ± 5	28.7 ± 0.2	1.02 ± 0.02	96 ± 10	25.7 ± 2.9	1.44 ± 0.05
PWD@-0.7V	**No BSA**	50 ± 4	20.9 ± 2.3	0.90 ± 0.05	63 ± 5	25.3 ± 1.8	1.25 ± 0.04
	BSA	60 ± 10	21.7 ± 3.3	0.95 ± 0.02	136 ± 29	24.4 ± 2.4	1.38 ± 0.08
PWD@-1.2V	**No BSA**	50 ± 5	21.7 ± 3.5	0.87 ± 0.13	62 ± 5	36.8 ± 3.6	1.51 ± 0.07
	BSA	57 ± 3	35.8 ± 6.9	0.98 ± 0.07	115 ± 42	35.7 ± 3.9	1.48 ± 0.16

*Deposition time at GE was 400s for all the gold deposited electrodes; the BSA concentrations used for biofouling are 40 mg•mL^{-1} and 2.0 mg•mL^{-1}for 3.0 mM $[Ru(NH_3)_6^{3+}]$ and 3.0 mM $[Fe(CN)_6^{4-}]$, respectively.

ΔE_p values suggest fast electron transfer [43].

3.5. Electrochemical kinetics of GE and GNS under different scan rates

Based on the previous results, we proceeded to further investigate the electrochemical behaviour of the electrodes by employing a diffusible redox mediator (3.0 mM $[Fe(CN)_6^{3-}]/[Fe(CN)_6^{4-}]$). Scan rate is a critical parameter for distinguishing between diffusion-controlled and thin-layer electrochemistry, where mass transfer is confined [44]. Varying the scan rate allowed us to study electron transfer kinetics by observing changes in peak intensities. Fig. 4A shows the CV curves of the unmodified GE and GNS-modified electrodes (fabricated at CPD@-0.7V, PWD@-0.7V, and PWD@-1.2V) as the scan rate was increased from 50 to 600 mV•s^{-1}.

To determine the mechanism governing the electrochemical reaction on each electrode, we plotted the logarithm of peak current (log I_p) versus the logarithm of scan rate (log v) for all electrodes (Fig. 4B). Specifically, we analysed the slope of the log I_p vs. log v, which indicates the dominant control mechanism. A slope of 0.5 or less reflects diffusion control, where reactants are transported from the bulk solution to the electrode surface. Slopes above 1.0 indicate adsorption control, dominated by surface-confined species, while values between 0.5 and 1.0 suggest a mixed regime involving both diffusion and adsorption processes. This oxidation (reduction) slope for unmodified GE was calculated to be 0.34 ± 0.09 (0.33 ± 0.05), indicating that the electron transfer mechanism was predominantly governed by a diffusion-controlled process. In contrast, the slopes for the various GNS-modified electrodes were as follows: 0.79 ± 0.01 (0.66 ± 0.01) for CPD@-0.7V, 0.63 ± 0.01 (0.51 ± 0.01) for PWD@-0.7V and 0.74 ± 0.00 (0.63 ± 0.01) for PWD@-1.2V. These values indicate that the redox reactions on the GNS-modified electrodes were governed by a combination of diffusion and adsorption or thin-layer diffusion-controlled processes.

Indeed, the voltammetric detection of ferrocyanide is a diffusion-limited reaction [14], because it drives a redox reaction with rapid electron transfer compared with the diffusion of species toward the surface. However, the surface roughness and the porosity of GNS will confine the diffusion process [45], which is the cause of deviations from purely diffusion-controlled behaviour. Therefore, thin-layer electrochemistry also contributed to the overall electron transfer mechanism [44], alongside classical diffusion processes. Pure-thin-layer behavior is the phenomenon where the analyte is confined within the nanostructure. As from the calculated slopes of log I_p *vs* log v in Fig. 4, it also demonstrated that the pine-needle shaped GNS exhibited a more significant deviation of slope at PWD@-1.2V(Slope of log I_p *vs* log $v = 0.74 \pm 0.00$) than that of PWD@-0.7V(Slope of log I_p *vs* log $v = 0.63 \pm 0.01$).

These thin-layer electrochemical effects, arising from analyte confinement within the porous GNS architecture, may also mitigate the impact of surface biofouling. Because a significant fraction of electroactive species resides within nanocavities less exposed to adsorbed foulants, the overall electrochemical response becomes less sensitive to surface blockage, offering a mechanistic explanation for the reduced

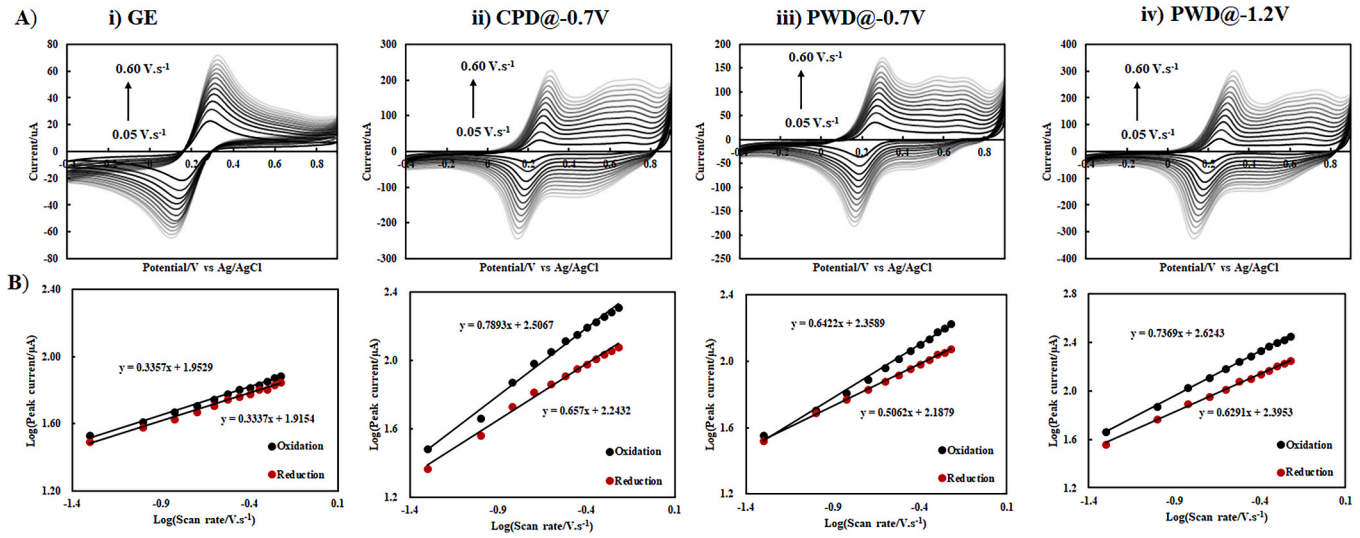

Fig. 4. **(A)** Cyclic voltammograms of 3.0 mM of $[Fe(CN)_6^{3-}]/[Fe(CN)_6^{4-}]$ at scan rates ranging from 0.05 to 0.60 V•s^{-1}. **(B)** Linear relationship between the logarithm of peak current and the logarithm of scan rate. Unmodified gold electrode (**i.** GE) and gold nanostructure modified electrodes (**ii.** CPD@-0.7V, **iii.** PWD@-0.7V and **iv.** PWD@-1.2V). (For interpretation of the references to colour in this figure legend, the reader is referred to the Web version of this article.)

fouling effects observed. Previous research provides further evidence that structure and mass transport are critical in antifouling [15]. Because large-scale surface roughness leads to thin layer electrochemistry when analyte is trapped in pores. Additionally, the anomalous Randles–Ševčík response [46] observed for these GNS-modified electrodes, maybe attributed to a thin-film liquid layer effect.

3.6. Bio-fouling performance of GNS using the OSR probe

Biofouling typically occurs on the electrode surface when it is exposed to biological media. The adsorption of protein from these media can lead to the formation of passivating multilayers on the sensing surface, ultimately resulting in unexpectedly low sensitivity. Therefore, it is important to investigate how different forms of GNS influence biofouling, in order to address the challenge of achieving higher ESAs while minimizing protein adsorption. The formation of nanoporous structures can restrict the diffusion of unwanted fouling proteins, although this same property may also hinder the access of target analytes [14].

In this study, BSA serves as a simplified model of the complex biofouling environment; however, such model systems are valuable for providing fundamental insights into the underlying phenomena. Moreover, the development of theoretical descriptions and computational models requires well-defined and controlled systems, which are necessarily simpler than realistic biological media. Therefore, the use of simplified systems should be prioritized as a crucial step toward establishing a mechanistic understanding that can later be extended to more complex environments. Thus, we compared the surface electron exchange rates of the electrodes using OSR and ISR probes in the absence and presence of BSA, a common biofouling agent. Biofouling has a markedly different impact on the redox kinetics of OSR and ISR probes at electrode surfaces [31]. The results of the biofouling studies on GNS-modified electrodes are shown in Fig. 5. Respective results for GNS-modified electrodes with 120 s deposition time are shown in Fig. S11A.

In these experiments by using the OSR probe, all the electrodes were immersed in a 3.0 mM $[Ru(NH_3)_6^{3+}]$ solution spiked with 40.0 mg•L^{-1} BSA for different durations: 0 h (measured immediately upon immersion), 0.5 h and 12 h. As shown in Fig. 5A, similar electrochemical behaviour was observed in the resulting CVs, with only minor changes in current intensity following BSA exposure for up to 12 h. The effect of BSA fouling on electrochemical behaviour was primarily reflected in ΔE_p variations, as presented in Table 1. BSA fouling had minimal impact on the $[Ru(NH_3)_6^{3+}]$ kinetics for all tested electrodes. The ΔE_p values for unmodified GE, CPD@-0.7V, and PWD@-0.7V and PWD@-1.2V after 0.5 h of BSA exposure remained within error margins of their respective pre-fouling values. Additionally, upon exposure to BSA, the I_{pa}/I_{pc} values for the OSR probe remained similar: 0.91 ± 0.00 for GE, 1.02 ± 0.02 for GNS (at CPD@-0.7V), 0.95 ± 0.02 for PWD@-0.7V, and 0.98 ± 0.07 for PWD@-1.2V. Notably, both the ΔE_p and I_{pa}/I_{pc} values remain consistent with a reversible electrochemical process for the OSR.

To better quantify the biofouling effect on the electrodes, SWV signals were recorded for OSR testing (see Fig. S12). The peak intensity in the absence of BSA was used as a reference to compare the electrochemical signals measured in the presence of BSA at various fouling durations. The ratio of the SWV peak intensity with BSA to that without BSA served as an indicator to evaluate the extent of biofouling for all tested electrode types (Fig. S11C).

Regarding the deposition time of 400 s, the SWV peak current ratios for CPD@-0.7V, PWD@-0.7V, and PWD@-1.2V increased notably, as shown in Fig. 6A. By the final measured time point of 36 h, these ratios had risen to approximately 1.86, 1.20, and 2.20, respectively. This substantial increase (ratios >1) can be attributed to the enhanced roughness and porosity, resulting in higher ESA, and denser GNS structures, allowing OSR probes to penetrate and become retained within the complex nanostructures. Beyond, from the raw data of SWV of GNS-based electrode in Fig. S12, we clearly noted that the baseline of the OSR probe signal was shifted to a lower value after long time biofouling, which was the main cause for an enhanced OSR redox signal. These findings support the same hypothesis presented in Section 3.2, namely that PWD@-1.2V allow for creating greater ESA and porosity than CPD@-0.7V and PWD@-0.7V.

3.7. Bio-fouling performance of GNS using the ISR probe

The biofouling effect on the ISR probe, $[Fe(CN)_6^{4-}]$, was investigated using a solution spiked with 2.0 mg•mL^{-1} BSA. $[Fe(CN)_6^{4-}]$ is often considered outersphere, but it is more surface-sensitive. A significant decrease in signal intensity was observed on GE immediately after immersion in the BSA-containing redox solution, confirming the rapid

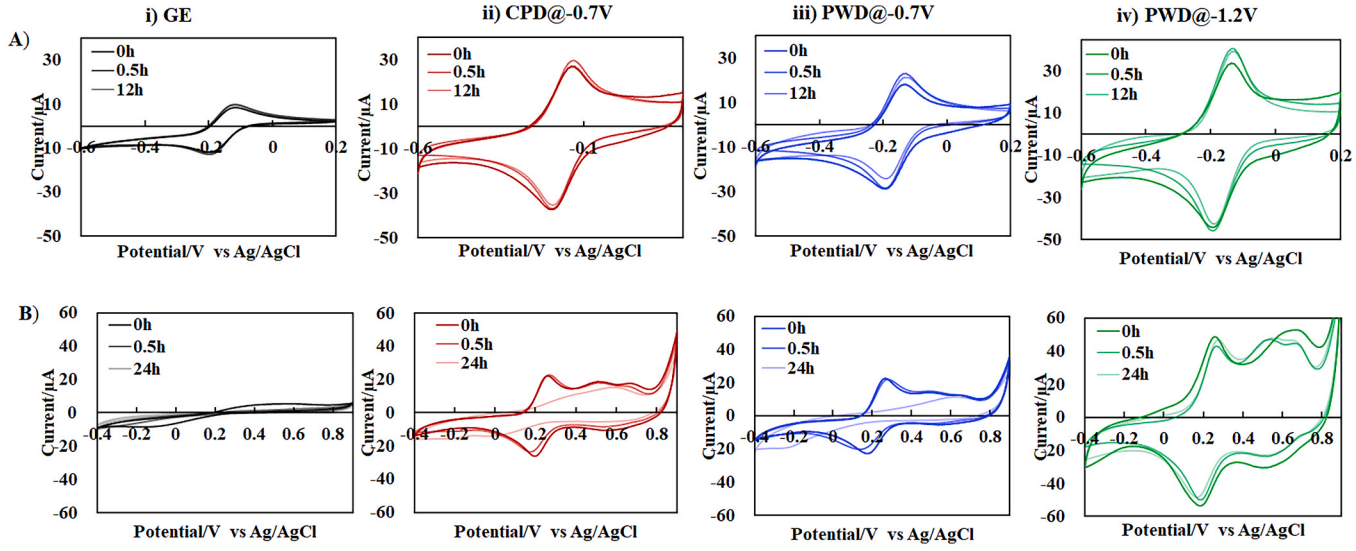

Fig. 5. Cyclic voltammogram characterization of biofouling process under different incubation time for the unmodified gold electrode (**i.** GE), and gold nanostructure–modified electrodes (**ii.** CPD@-0.7 V, **iii.** PWD@-0.7 V and **iv.** PWD@-1.2 V). **A)** Cyclic voltammograms in 3.0 mM $[Ru(NH_3)_6^{3+}]$ with 40.0 mg • mL^{-1} BSA, at 0 h, 0.5 h and 12 h, and **B)** 3.0 mM $[Fe(CN)_6^{4-}]$ with 2.0 mg • mL^{-1} BSA, at 0 h, 0.5 h and 24 h. (For interpretation of the references to colour in this figure legend, the reader is referred to the Web version of this article.)

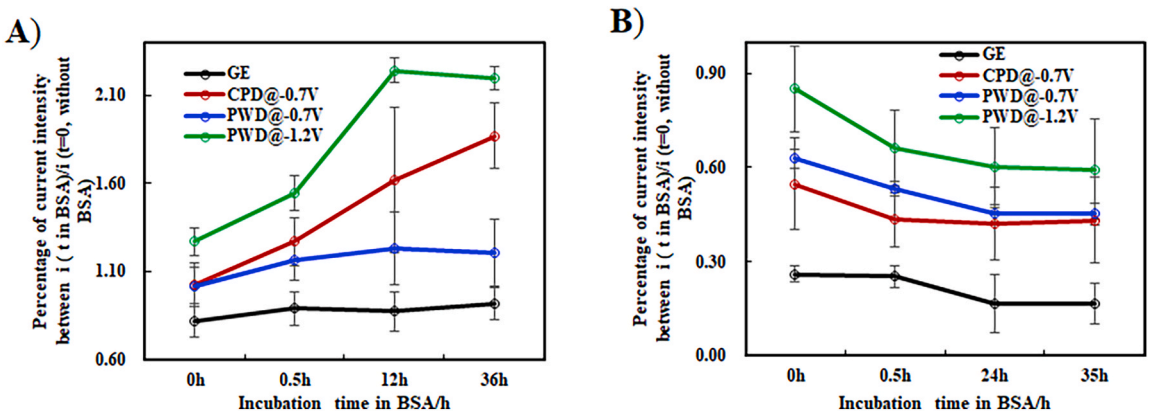

Fig. 6. Biofouling performance of unmodified gold electrode (**i.** GE) and gold nanostructured modified electrodes (**ii.** CPD@-0.7 V, **iii.** PWD@-0.7 V and **iv.** PWD@-1.2 V) **A)** Square wave voltammetry peak current intensity in 3.0 mM $[Ru(NH_3)_6^{3+}]$ in the presence of 40.0 mg • mL^{-1} BSA over time (0 h, 0.5 h, 12 h and 36 h), compared to peak intensity in the absence of BSA and **B)** in 3.0 mM $[Fe(CN)_6^{4-}]$ in the presence of 2.0 mg • mL^{-1} BSA over time (0 h, 0.5 h, 24 h and 35 h), compared to peak intensity in the absence of BSA. (For interpretation of the references to colour in this figure legend, the reader is referred to the Web version of this article.)

impact of BSA and the lack of antibiofouling properties. BSA adsorption on the GE surface markedly hindered electron transfer, resulting in less defined CV curve peaks, decreased peak current and increased ΔE_p. To further assess the impact of exposure duration, the electrodes were incubated in the biofouling solution for 0.5 h and 24 h (Fig. 5B). After 0.5 h of incubation, the CV signal on GE became nearly flat, and ΔE_p could no longer be determined. Notably, the impact of BSA was particularly pronounced for $[Fe(CN)_6^{4-}]$, where ΔE_p became undetectable on the unmodified surface, in contrast to the relatively smaller effect observed with $[Ru(NH_3)_6^{3+}]$ kinetics.

This enhanced antifouling behavior was first evident in the CV signals, which showed nearly identical peak shapes and intensities in both the absence and immediate presence of BSA (0 h) (Fig. 5B). As shown in Fig. 5B ii-iv, the CV peaks for **ii)** CPD@-0.7V, **iii)** PWD@-0.7V and **iv)** PWD@-1.2V, remained nearly unchanged after 0.5 h of BSA exposure. As displayed in Fig. S13, we noted that for these tested electrodes, the BSA fouling impacted on the ISR probe signal was a rapid process with a time resolution of minutes. While the electrodes of CPD@-0.7V and PWD@-0.7V reached their balance within 5 min, the sample of PWD@-1.2V took 30 min to reach a balance status. Particularly, the unmodified GE became a balance ISR redox signal within a minute. Indeed, the GNS-modified electrodes demonstrated improved antifouling performance, as their CVs retained peak shapes comparable to those recorded in BSA-free solutions, with no significant shifts in ΔE_p (Table 1). The corresponding ΔE_p values after BSA fouling were 96 ± 10 mV (increased by 68.4 %) for CPD@-0.7V, 136 ± 29 mV (increased by 115.9 %) for PWD@-0.7V, and 115 ± 42 mV (increased by 85.5 %) for PWD@-1.2V, as presented in Table 1. Although Faradaic current weakening was observed for CPD@-0.7V and PWD@-0.7V after 24 h, the PWD@-1.2V electrode demonstrated notably superior antifouling performance, maintaining stable CV signals even after prolonged exposure. This highlights the enhanced biofouling resistance of the PWD@-1.2V electrode, likely due to its higher ESA and optimized pine-needle morphology.

Similarly, the same approach was applied in the SWV studies using the BSA-spiked ISR probe (see Fig. S14). In contrast to the OSR results, SWV peak current ratios decreased over the 35 h BSA exposure period for all tested electrode types (Fig. S11D), and from Fig. S14, we noted that the decrease of the ISR redox signal was mainly caused by the reduction of the peak signal during the biofouling process. Although the SWV peak current ratio for the unmodified GE dropped to approximately 0.17 after 35 h of BSA exposure, the SWV peak current ratios are significantly better for these GNS-modified electrodes. As shown in Fig. 6B, their values were estimated to be 0.43 (CPD@-0.7V), 0.45 (PWD@-0.7V), and 0.59 (PWD@-1.2V).

Because the ESA and the gold morphology were the two key parameters, contributing to an enhanced antifouling performance. To clarify this question, we summarized all antifouling performances of the tested electrodes in Fig. 7. As we described in both sections 3.6 and 3.7, the ratio of measured redox intensity with and without the existence of the BSA was the indicator for the antifouling performance, which showed the remaining redox signal after electrode fouling. Typically, their antifouling performance were enhanced with the increase of their ESA for both pine-needle-shaped GNS or coral-shaped GNS electrodes. However, it is clearly observed that the pine-needle-shaped GNS has their priority in contributing to the antifouling performance, compared to that of the coral-shaped GNS. To minimize the impact of ESA on the biofouling performance, we mainly compared similar ESAs for the biofouling performance investigated in this study. At comparable ESAs of 4.30 and 3.84, achieved through CPD@-0.7V(120s) and PWD@-1.2V (120s), similar biofouling performance was observed. Meanwhile, their SWV peak current ratios were nearly identical, 0.36 and 0.35, respectively. Additionally, we compared the biofouling performance of CPD@-1.0V(120s) and PWD@-0.7V(400s), which had similar ESAs of

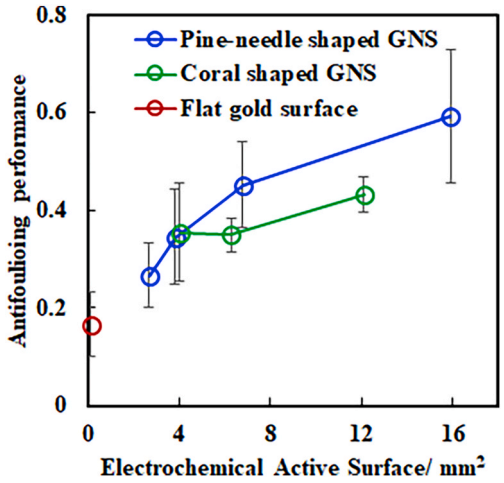

Fig. 7. Antifouling performance comparison of the Pine-needle-shaped GNS, Coral-shaped GNS and Flat gold surface. The measurements were performed with BSA at 2.0 mg • mL^{-1} and 3.0 mM $[Fe(CN)_6^{3-}]$, and all electrodes were incubated for up to 35h to assess biofouling. (For interpretation of the references to colour in this figure legend, the reader is referred to the Web version of this article.)

6.27 and 6.80 mm^2, respectively. Notably, PWD@-0.7V(400s) showed a better performance, with a higher SWV ratio of 0.45, compared to 0.35 for CPD@-0.7V(120s). This result suggests that the unique structure of pine needle GNS (fabricated by PWD) itself contributed to the enhanced antifouling performance (increased 22 %), beyond the influence of its ultra-high ESA.

Furthermore, although a longer deposition time was critical for achieving higher ESAs, these nanostructures, fabricated using the PWD method, inherently demonstrated superior performance compared to those prepared by the CPD method.

Of note, introducing a third probe with different electron-transfer kinetics and inner-sphere interaction mechanisms (such as catechols) would provide further insight beyond what is covered here, owing to their strong surface sensitivity and propensity for adsorption. Therefore, we deliberately limited our study to two well-established, classical redox probes hexamine ruthenium chloride and potassium ferricyanide in the present work. Because our aim is not to exhaustively catalogue all possible charge and adsorption scenarios, but to demonstrate that probe charge leads to qualitatively different trends under BSA adsorption and porous electrode conditions. And we believe this is sufficiently evidenced by the two complementary systems studied.

To obtain direct evidence of the antifouling performance of these surfaces, complementary analysis using QCM would be valuable. Moreover, from an application perspective, not only the amount of adsorbed proteins but also their orientation plays a critical role. Therefore, additional characterization techniques, such as polarized ATR-FTIR spectroscopy, are needed to elucidate protein adsorption orientation and interfacial structure.

While numerous antifouling gold nanostructures, such as dendritic, flowerlike, and nanoporous morphologies, have been reported, direct comparison across studies is inherently difficult due to the lack of standardized fabrication and testing protocols. Antifouling performance is strongly influenced not only by morphology but also by factors such as electrode geometry, the characteristics of the redox probe, and the conditions used during fouling assays, all of which vary widely in the literature. In this work, we therefore restricted our comparison to structures produced under tightly controlled and directly comparable conditions, altering only the deposition mode (PWD vs. CPD). This approach enabled us to isolate the effect of morphology and electroactive surface area on antifouling behaviour without confounding variables. Future systematic studies employing harmonized fabrication and evaluation conditions would be valuable for establishing a reliable performance baseline across different gold nanostructures.

Our pine-needle–like structures demonstrated markedly strong antifouling behaviour and preserved electrochemical activity even in the presence of BSA. Their high electroactive surface area combined with the highly branched, anisotropic features likely mitigates surface blocking and enables analyte access despite partial protein adsorption.

While further investigations in more complex environments (e.g., fibrinogen, serum/plasma, saliva) are needed to validate the universal antifouling performance of the needle-like structure, BSA serves as a simplified model of the biofouling environment. Such model systems are valuable for providing fundamental insights into the underlying phenomena. Moreover, the development of theoretical descriptions and computational models requires well-defined and controlled systems, which are necessarily simpler than realistic biological media. Therefore, the use of simplified systems should be prioritized as a crucial step toward establishing a mechanistic understanding that can later be extended to more complex environments.

4. Conclusions

The aim of this study was to test how the constructional differences of GNS on electrodes surfaces impact antifouling and electrochemical performance. Completely distinct types of GNSs were deposited electrochemically by applying low potentials (0, −0.3, and −0.7 V), using the deposition modes of CPD. However, by applying higher deposition potentials (over −1.0 V) under the CPD process, the resulting GNS structures became increasingly identical. Thus, another deposition mode of PWD was chosen for −1.2 V (as well as −0.7 V), to obtain their distinct GNS, in terms of experimenting with higher PWD deposition potentials. Compared to that of CPD method, PWD enabled gold deposits to form pine-needle-shaped GNS. According to the surface and electrochemical characterization, it was observed that GNS deposition significantly increased ESA and surface roughness.

As deposition model and voltages played a critical role in resulting in a rich and dense porous nanomaterial structure on the electrode surface, we chose the ESA parameter as the indicator for every fabricated electrode here. Interestingly, we demonstrated that all the fabricated electrodes by using both CPD and PWD, followed the same tendency between the ESA and their electrochemical responses. As such, the electrochemical responses of the OSR probe indicated that the optimal ESA observed in the GNS structures was 2.68 ± 0.56 mm^2. Transitioning to ultra-high ESAs was associated with an increase in capacitive current, which in turn led to a reduction in OSR intensity. For the ISR probe, the intensity was observed to strongly depend on the ESA, although the values became more convergent as the ESA approached 6.27 ± 1.20 mm^2.

However, over-deposition of GNS upon the GE also caused a slight reduction of the electrochemical response to ISR probes. Over-deposited PWD@-1.2V(400s) showed the highest antifouling performance, with an ISR signal ratio of 0.59 ± 0.16, compared to 0.43 ± 0.14 for GNS (at CPD@-0.7V(400s)) and 0.45 ± 0.04 for PWD@-0.7V(400s). Clearly, our results demonstrated that pine-needle-shaped GNS effectively inhibited the formation of a BSA fouling layer while simultaneously enhancing the electrode's electrochemical performance.

To conclude and summarize, the advancements in the design and performance of GNS highlight the pivotal role of material science in electrochemical biomedical sensing, paving the way for cost-effective and easily fabricated sensors. This study provided a detailed analysis of the antifouling performance and electrochemical properties of various GNSs, identifying pine-needle-shaped GNS as a particularly promising candidate for biomedical sensing in complex biofluids. The enhanced electron transfer kinetics, combined with the porous structures of GNS, and amplified electrochemical signals, created an effective size-exclusion mechanism to prevent biofouling. These properties allowed the modified electrodes to maintain high sensitivity even in biological fluids with high concentrations of contaminating proteins. Overall, this work lays a solid foundation for designing and fabricating GNS with increasingly complex and hierarchical structures, offering significant potential for applications in healthcare diagnostics, biomedical sensing, and environmental monitoring.

CRediT authorship contribution statement

Feixiong Chen: Writing – original draft, Project administration, Methodology, Investigation, Funding acquisition, Formal analysis, Data curation, Conceptualization. **Bahar Mostafiz:** Writing – review & editing, Investigation. **Emilia Peltola:** Writing – review & editing, Funding acquisition, Supervision, Resources.

Availability of data and materials

The data are available from the corresponding author upon reasonable request.

Ethics approval and consent to participate

There is no ethical issue in this study.

Consent for publication

Not applicable.

Fundings

We acknowledge funding from The Research Council of Finland under the Scientific Council for Natural Sciences and Engineering with project No. 347021, 352421, 352899 and 355747. FC acknowledges the Proof-of-Concept (PoC) funding 2025 from the University of Oulu and the City of Oulu with project No.24305099116. FC acknowledges 6GESS research programme funding from the University of Oulu with project No. 246301001372. The work was conducted under the #SUSMAT umbrella.

Declaration of competing interest

The authors declare that they have no known competing financial interests or personal relationships that could have appeared to influence the work reported in this paper.

Acknowledgments

We acknowledge the great support from Dr. Ilari Angervo (Wihuri Physical Laboratory, Department of Physics and Astronomy, University of Turku, Finland) for XRD testing of our samples, and from Dr. Sari Granroth (Department of Physics and Astronomy, University of Turku, 20014, Turku, Finland) for XPS measurement of our samples.

Appendix A. Supplementary data

Supplementary data to this article can be found online at https://doi.org/10.1016/j.aca.2025.345022.

Data availability

Data will be made available on request.

References

[1] M. Ghaani, M. Azimzadeh, D. Büyüktaş, D. Carullo, S. Farris, Electrochemical sensors in the food sector: a review, J. Agric. Food Chem. 72 (2024) 24170–24190, https://doi.org/10.1021/acs.jafc.4c09423.
[2] A. Barhoum, S. Hamimed, H. Slimi, A. Othmani, F.M. Abdel-Haleem, M. Bechelany, Modern designs of electrochemical sensor platforms for environmental analyses: principles, nanofabrication opportunities, and challenges, Trends Environ. Anal. Chem. 38 (2023) e00199, https://doi.org/10.1016/j.teac.2023.e00199.
[3] G.C. Biswas, S. Choudhury, M.M. Rabbani, J. Das, A review on potential electrochemical point-of-care tests targeting pandemic infectious disease detection: COVID-19 as a reference, Chemosensors. 10 (2022) 269, https://doi.org/10.3390/chemosensors10070269.
[4] J. Kim, J. Jeong, S.H. Ko, Electrochemical biosensors for point-of-care testing, bio-design, Manuf. 7 (2024) 548–565, https://doi.org/10.1007/s42242-024-00301-6.
[5] F. Chen, N. Haddour, M. Frenea-Robin, Y. Chevolot, V. Monnier, Electroactive magnetic nanoparticles under magnetic attraction on a microchip electrochemical device, J. Magn. Magn Mater. 475 (2019) 345–351, https://doi.org/10.1016/j.jmmm.2018.11.091.
[6] C. Zhu, G. Yang, H. Li, D. Du, Y. Lin, Electrochemical sensors and biosensors based on nanomaterials and nanostructures, Anal. Chem. 87 (2015) 230–249, https://doi.org/10.1021/ac5039863.
[7] F. Chen, B. Mostafiz, J. Suni, E. Peltola, Electrochemical design of gold nanostructures for controllable electrochemical performance and scalable aptamer sensing application, ACS Appl. Nano Mater. 8 (2025) 9812–9823, https://doi.org/10.1021/acsanm.5c00962.
[8] N. Liu, Z. Xu, A. Morrin, X. Luo, Low fouling strategies for electrochemical biosensors targeting disease biomarkers, Anal. Methods. 11 (2019) 702–711, https://doi.org/10.1039/c8ay02674b.
[9] D.P. Carroll, P.M. Mendes, Recent advances in surface modification and antifouling strategies for electrochemical sensing in complex biofluids, Curr. Opin. Electrochem. 40 (2023) 101319, https://doi.org/10.1016/j.coelec.2023.101319.
[10] P.H. Lin, B.R. Li, Antifouling strategies in advanced electrochemical sensors and biosensors, Analyst. 145 (2020) 1110–1120, https://doi.org/10.1039/c9an02017a.
[11] G. Chen, W. Chen, L. Xu, H. Jin, W. Sun, J. Lan, F. Wu, X. Zhang, J. Zhang, J. Chen, Sensitive, highly stable, and anti-fouling electrode with hexanethiol and Poly-A modification for exosomal microRNA detection, Anal. Chem. 94 (2022) 5382–5391, https://doi.org/10.1021/acs.analchem.2c00069.
[12] L. Qi, R. Liang, T. Jiang, W. Qin, Anti-fouling polymeric membrane ion-selective electrodes, TrAC, Trends Anal. Chem. 150 (2022) 116572, https://doi.org/10.1016/j.trac.2022.116572.
[13] L. Zhou, X. Li, B. Zhu, B. Su, An overview of antifouling strategies for electrochemical analysis, Electroanalysis. 34 (2022) 966–975, https://doi.org/10.1002/elan.202100406.
[14] J. Sabaté del Río, H.K. Woo, J. Park, H.K. Ha, J.R. Kim, Y.K. Cho, SEEDING to enable sensitive electrochemical detection of biomarkers in undiluted biological samples, Adv. Mater. 34 (2022) 2200981, https://doi.org/10.1002/adma.202200981.
[15] A. Kousar, E. Peltola, T. Laurila, Nanostructured geometries strongly affect fouling of carbon electrodes, ACS Omega. 6 (2021) 26391–26403, https://doi.org/10.1021/acsomega.1c03666.
[16] J. Sabaté, O.Y.F. Henry, P. Jolly, D.E. Ingber, An antifouling coating that enables affinity-based electrochemical biosensing in complex biological fluids, Nat. Nanotechnol. 14 (2019) 1143–1149.
[17] E. González-Martínez, S. Saem, N.E. Beganovic, J.M. Moran-Mirabal, Electrochemical nano-roughening of gold microstructured electrodes for enhanced sensing in biofluids, Angew. Chem. Int. Ed. 62 (2023) e202218080, https://doi.org/10.1002/anie.202218080.
[18] S. Guo, L. Wang, E. Wang, Templateless, surfactantless, simple electrochemical route to rapid synthesis of diameter-controlled 3D flowerlike gold microstructure with "clean" surface, Chem. Commun. 3 (2007) 3163–3165, https://doi.org/10.1039/b705630c.
[19] L. Soleymani, Z. Fang, B. Lam, X. Bin, E. Vasilyeva, A.J. Ross, E.H. Sargent, S. O. Kelley, Hierarchical nanotextured microelectrodes overcome the molecular transport barrier to achieve rapid, direct bacterial detection, ACS Nano. 5 (2011) 3360–3366, https://doi.org/10.1021/nn200586s.
[20] C. Zhu, G. Meng, Q. Huang, Z. Huang, Z. Chu, Au hierarchical micro/nanotower arrays and their improved SERS effect by Ag nanoparticle decoration, Cryst. Growth Des. 11 (2011) 748–752, https://doi.org/10.1021/cg101266d.
[21] P. Sadat Mousavi, S.J. Smith, J.B. Chen, M. Karlikow, A. Tinafar, C. Robinson, W. Liu, D. Ma, A.A. Green, S.O. Kelley, K. Pardee, A multiplexed, electrochemical interface for gene-circuit-based sensors, Nat. Chem. 12 (2020) 48–55, https://doi.org/10.1038/s41557-019-0366-y.
[22] B. Seo, S. Choi, J. Kim, Simple electrochemical deposition of Au nanoplates from Au(I) cyanide complexes and their electrocatalytic activities, ACS Appl. Mater. Interfaces. 3 (2011) 441–446, https://doi.org/10.1021/am101018g.
[23] E. Rafatmah, B. Hemmateenejad, Dendrite gold nanostructures electrodeposited on paper fibers: application to electrochemical non-enzymatic determination of glucose, Sensor. Actuator. B Chem. 304 (2020) 127335, https://doi.org/10.1016/j.snb.2019.127335.
[24] Y. Xia, J. Liu, W. Huang, Z. Li, Electrochemical fabrication of clean dendritic Au supported Pt clusters for electrocatalytic oxidation of formic acid, Electrochim. Acta 70 (2012) 304–312, https://doi.org/10.1016/j.electacta.2012.03.071.
[25] N. German, A. Ramanavicius, A. Ramanaviciene, Electrochemical deposition of gold nanoparticles on graphite rod for glucose biosensing, Sensor. Actuator. B Chem. 203 (2014) 25–34, https://doi.org/10.1016/j.snb.2014.06.021.
[26] Y. Tian, H. Liu, G. Zhao, T. Tatsuma, Shape-controlled electrodeposition of gold nanostructures, J. Phys. Chem. B 110 (2006) 23478–23481, https://doi.org/10.1021/jp065292q.
[27] R. Herrala, K. Yliniemi, J. Vapaavuori, M. Lundström, Selective gold recovery with electrochemically assisted aqueous reduction, J. Sustain. Metall. 11 (2025) 1214–1225, https://doi.org/10.1007/s40831-025-01048-9.
[28] A.J. Ritz, O.M. Stuehr, D.N. Comer, R.A. Lazenby, Controlling gold morphology using electrodeposition for the preparation of electrochemical aptamer-based sensors, ACS Appl. Bio Mater. 7 (2024) 1925–1935, https://doi.org/10.1021/acsabm.3c01254.
[29] J. Lin, M. Kilani, M. Baharfar, R. Wang, G. Mao, Understanding the nanoscale phenomena of nucleation and crystal growth in electrodeposition, Nanoscale. (2024) 19564–19588, https://doi.org/10.1039/d4nr02389g.
[30] E. Peltola, S. Sainio, K.B. Holt, T. Palomäki, J. Koskinen, T. Laurila, Electrochemical fouling of dopamine and recovery of carbon electrodes, Anal. Chem. 90 (2018) 1408–1416, https://doi.org/10.1021/acs.analchem.7b04793.
[31] E. Peltola, A. Aarva, S. Sainio, J.J. Heikkinen, N. Wester, V. Jokinen, J. Koskinen, T. Laurila, Biofouling affects the redox kinetics of outer and inner sphere probes on carbon surfaces drastically differently-implications to biosensing, Phys. Chem. Chem. Phys. 22 (2020) 16630–16640, https://doi.org/10.1039/d0cp02251a.
[32] C. Wu, A. Offenhäusser, D. Mayer, A highly sensitive amperometric aptamer biosensor for adenosine triphosphate detection on a 64 channel gold multielectrode array, Phys. Status Solidi Appl. Mater. Sci. 217 (2020) 1–8, https://doi.org/10.1002/pssa.201900925.
[33] A. Kumar, J.M. Gonçalves, A. Sukeri, K. Araki, M. Bertotti, Correlating surface growth of nanoporous gold with electrodeposition parameters to optimize amperometric sensing of nitrite, Sensor. Actuator. B Chem. 263 (2018) 237–247, https://doi.org/10.1016/j.snb.2018.02.125.
[34] B. Ren, L.A. Jones, M. Chen, D.K. Oppedisano, D. Qiu, S.J. Ippolito, S.K. Bhargava, The Effect of Electrodeposition Parameters and Morphology on the Performance of Au Nanostructures for the Detection of As (III), J. Electrochem. Soc. 164 (2017) H1121–H1128, https://doi.org/10.1149/2.1261714jes.

[35] H.C. Shin, J. Dong, M. Liu, Nanoporous structures prepared by an electrochemical deposition process, Adv. Mater. 15 (2003) 1610–1614, https://doi.org/10.1002/adma.200305160.
[36] M. Imran Hossain, A. Dutta, J. Ahmed, M. Faisal, J.S. Algethami, F.A. Harraz, M. A. Hasnat, Electroless deposition of gold on a glassy carbon electrode (GCE) surface for selective detection of hydrogen peroxide, ChemistrySelect 9 (2024) e202301638, https://doi.org/10.1002/slct.202301638.
[37] D. Sah, Chitra, K. Lodhi, C. Kant, S.K. Srivastava, S. Kumar, Extraction and analysis of recovered silver and silicon from laboratory grade waste solar cells, Silicon. 14 (2022) 9635–9642, https://doi.org/10.1007/s12633-022-01715-6.
[38] T.T.K. Chi, N.T. Le, B.T.T. Hien, D.Q. Trung, N.Q. Liem, Preparation of SERS substrates for the detection of organic molecules at low concentration, Commun. Phys. 26 (2017) 261, https://doi.org/10.15625/0868-3166/26/3/8053.
[39] S. Budi, A. Auliya, S. Winarsih, M.H. Fauzi, N. Yusmaniar, Square-wave pulse electrodeposition of gold nanoparticles for ethanol electrooxidation, Mater. Adv. 4 (2023) 5556–5563, https://doi.org/10.1039/d3ma00412k.
[40] Z. Li, Z. Guo, Bioinspired surfaces with wettability for antifouling application, Nanoscale 11 (2019) 22636–22663, https://doi.org/10.1039/c9nr05870b.
[41] D. Menshykau, I. Streeter, R.G. Compton, Influence of electrode roughness on cyclic voltammetry, J. Phys. Chem. C 112 (2008) 14428–14438, https://doi.org/10.1021/jp8047423.
[42] D. Menshykau, R.G. Compton, The influence of electrode porosity on diffusional cyclic voltammetry, Electroanalysis. 20 (2008) 2387–2394, https://doi.org/10.1002/elan.200804334.
[43] C. Costentin, Cyclic voltammetry to study dynamics of ion insertion in porous materials, Adv. Energy Sustain. Res. 5 (2024) 1–11, https://doi.org/10.1002/aesr.202300242.
[44] Q. Cao, Z. Shao, D.K. Hensley, N.V. Lavrik, B.J. Venton, Influence of geometry on thin layer and diffusion processes at carbon electrodes, Langmuir. 37 (2021) 2667–2676, https://doi.org/10.1021/acs.langmuir.0c03315.
[45] E. Leppanen, M. Akhoundian, S. Sainio, J. Etula, O. Pitkanen, T. Laurila, Structure-property relationships in carbon electrochemistry, Carbon N. Y. 200 (2022) 375–389, https://doi.org/10.1016/j.carbon.2022.08.076.
[46] P. Rama Kant, Theory for staircase voltammetry and linear scan voltammetry onfractal electrodes: emergence of anomalous Randles-Sevcik behavior, Electrochim. Acta. 111 (2013) 223–233, https://doi.org/10.1016/j.electacta.2013.07.163.